Spectrum of Engineering Sciences
ISSN (e) 3007-3138 (p) 3007-312X Volume 4, Issue 4, 2026

# SYNTHESIS OF ZN DOPED MAGHEMITE BY WET CHEMICAL APPROACH FOR POTENTIAL DESULFURIZATION STUDY OF PAKISTANI DIESEL FUEL

**Adil[*1], Danish Raza[2], Syed Farhan Hasany[3], Sajid Hussain[4]**

[*1]*Department of Physics NED University of Engineering and Technology, Karachi, Pakistan*
[2]*Department of Chemistry NED University of Engineering and Technology, Karachi, Pakistan*
[3]*Institute of Industrial Electronics Engineering, Karachi, Pakistan*

[*1]adilkhanindus@gmail.com

DOI: https://doi.org/10.5281/zenodo.19807973

**Keywords**
*Maghemite, Zn-doped, Nanocatalysts, Redox activity, Diesel*

**Article History**
*Received: 26 February 2026*
*Accepted: 06 April 2026*
*Published: 27 April 2026*


**Corresponding Author: ***
**Adil**

**Abstract**

*Maghemite ($\gamma$-$Fe_2O_3$) nanoparticles and Zn-doped maghemite nanomaterials were synthesized with controlled size to investigate the influence of $Zn^{2+}$ incorporation on structural, magnetic, and catalytic properties. X-ray diffraction confirmed the formation of a single-phase cubic spinel structure with successful Zn substitution, accompanied by lattice distortion and variation in crystallite size. Magnetic measurements revealed superparamagnetic behavior for all samples, with a gradual decrease in saturation magnetization due to cation redistribution and weakening of $Fe^{3+}$–O–$Fe^{3+}$ superexchange interactions upon Zn doping. Morphological analysis indicated quasi-spherical nanoparticles with nanoscale aggregation.*

*The catalytic performance was evaluated via oxidative desulfurization of diesel using $H_2O_2$ as an oxidant. Zn doping significantly enhanced sulfur removal efficiency, reaching up to ~65%, attributed to increased defect density, improved redox activity, and enhanced adsorption of sulfur compounds. Furthermore, the catalysts demonstrated efficient magnetic recovery and reusability. The study establishes a clear structure property performance relationship, highlighting Zn-doped maghemite nanoparticles as significant, efficient, and recyclable nanocatalysts for environmental remediation applications.*

## 1. INTRODUCTION:

Maghemite ($\gamma$-$Fe_2O_3$) is a technologically significant magnetic iron oxide that has attracted considerable attention due to its versatile physicochemical properties and wide range of applications (Dhahri et al., 2025). Among magnetic nanomaterials, maghemite is particularly valued for its role as the magnetic phase in ferrofluids (Halbreich et al., 1998), which are extensively utilized in biomedical and engineering systems (Khan, Gupta, & Verma, 2013), including targeted drug delivery, magnetic resonance imaging (MRI), and sealing technologies (Bruno et al., 2022). Its excellent chemical stability, low toxicity, and inherent biocompatibility further enable its application in solid-phase extraction (Bashir & Shahid, 2026), diagnostic imaging, and hyperthermia-based cancer therapy, where localized heating under an alternating magnetic field is exploited for tumor ablation (Skandalakis et al., 2020).

Structurally, maghemite belongs to the inverse spinel family and can be described by a vacancy-ordered framework, typically represented as;

$$(Fe^{3+})Fe5/3^{3+}\ \square 1/_{3}O_4$$

Where vacancies are predominantly located at octahedral (B) sites. This intrinsic vacancy-rich structure distinguishes maghemite from magnetite ($Fe_3O_4$) and contributes to its enhanced chemical and thermal stability (Ahamed, Ali, Lateef, Dotto, & Alhadlaq). Upon thermal treatment at elevated temperatures, maghemite undergoes a phase transformation into hematite ($\alpha$-$Fe_2O_3$), which is the thermodynamically stable phase (Duglet, Sharma, Singh, Sharma, & Singh, 2025). According to Néel's two-sublattice model, the magnetic behavior of maghemite arises from antiparallel alignment of magnetic moments in tetrahedral (A) and octahedral (B) sites (Khanvilkar et al., 2023) , resulting in ferrimagnetism with a high saturation magnetization close to experimentally observed values (Lee et al., 2022).

One of the key advantages of maghemite over magnetite lies in its structural vacancies, which facilitate the incorporation of divalent or multivalent cations into the lattice (Ahmed & Sanad, 2021). This tunability enables the design of doped ferrite systems with tailored magnetic, electronic, and catalytic properties (Ahmed & Sanad, 2021). In (Al Kindi, 2020)particular, spinel ferrites with the general formula $MFe_2O_4$ (where M = $Zn^{2+}$, $Co^{2+}$, $Mn^{2+}$, $Mg^{2+}$, $Ni^{2+}$, etc.) have gained significant attention due to their remarkable combination of ferrimagnetic and semiconducting behavior (Ahmed & Sanad, 2021). These materials have been widely explored for applications in sensors, magnetic storage devices, microwave technologies, catalysis, and biomedical systems, including drug delivery and hyperthermia (Aflori, 2021).

At the nanoscale, ferrite materials exhibit unique properties arising from quantum confinement effects and high surface-to-volume ratios (Aflori, 2021). As particle size decreases to the single-domain regime, magnetic nanoparticles exhibit superparamagnetic behavior, characterized by negligible coercivity and remanence (Nisticò, Cesano, & Garello, 2020). This property is particularly advantageous for biomedical and catalytic applications, as it allows for efficient magnetic separation without residual magnetization (Anik et al., 2021). However, surface spin canting and structural disorder in nanoparticles often lead to reduced magnetization compared to bulk counterparts, emphasizing the importance of controlled synthesis and compositional tuning (Ma, Mohapatra, Wei, Liu, & Sun, 2021).

Among various dopants, $Zn^{2+}$ ions play a crucial role in modifying the magnetic and structural properties of spinel ferrites (Ma et al., 2021). $Zn^{2+}$ preferentially occupies tetrahedral (A) sites, leading to cation redistribution and alteration of superexchange interactions between A and B sites. At low concentrations (Mazen, Abu-Elsaad, & Nawara, 2020), Zn substitution can enhance magnetization by optimizing cation distribution, whereas higher concentrations may dilute magnetic interactions and reduce overall magnetization. Additionally, Zn incorporation introduces lattice distortion and defects, which can significantly influence catalytic activity by increasing the density of active sites (Castellanos-Rubio et al., 2021).

The synthesis route plays a vital role in determining the structural and functional properties of ferrite nanoparticles. Various methods, including co-precipitation, microemulsion (Islam, Pavel, Islam, & Haque, 2022), thermal decomposition, and oxidation of magnetite, have been employed for the preparation of maghemite nanoparticles. Among these, the sol–gel method has emerged as a highly effective and versatile approach, offering precise control over stoichiometry, phase purity, and particle size distribution (Salih & Mahmood, 2023). The sol–gel process enables homogeneous nucleation and growth, resulting in uniform nanoparticles with enhanced reproducibility (Bokov et al., 2021). Compared to metal–organic routes, the inorganic sol–gel approach using metal salts is more cost-effective and easier to handle, although it may involve challenges related to by-product formation and reaction control (Khandaker et al., 2025).

Recent advances in nanotechnology have further expanded the application scope of magnetic nanoparticles, particularly in catalysis and environmental remediation (Chaudhari et al., 2024). The incorporation of transition metal ions into maghemite not only modifies its magnetic behavior but also enhances its catalytic efficiency through improved redox properties and surface reactivity (Elmacı, Özgenç, Kurz, & Zumreoglu-Karan, 2020). In oxidative processes, such as desulfurization, doped ferrites facilitate the activation of oxidants and promote the conversion of sulfur-containing compounds into easily removable oxidized species (Mugisha, 2024).

In light of the growing demand for efficient and magnetically recoverable nanocatalysts, the present study is designed to systematically develop and evaluate maghemite-based nanomaterials with controlled physicochemical properties. Firstly, size-controlled γ-$Fe_2O_3$ nanoparticles are synthesized to establish a baseline for structural and magnetic characteristics. Subsequently, Zn-doped maghemite nanomaterials with tunable particle size and composition are prepared to investigate the influence of $Zn^{2+}$ incorporation on lattice structure, magnetic behavior, and surface reactivity. Finally, the catalytic potential of these materials is explored in oxidative desulfurization of diesel fuel, with particular emphasis on process optimization and efficient catalyst recovery via magnetic separation. This integrated approach aims to establish a clear structure–property–performance relationship, enabling the development of highly efficient and recyclable nanocatalysts for environmental remediation applications.

## 2. Methodology:

### 2.1 Preparation steps of maghemite nanoparticles:

Maghemite nanoparticles are prepared by sol-gel method. The method includes following major steps;

I. Hydrolysis
II. Condensation
III. Calcination process

**2.1.1 Hydrolysis:** The formation of Maghemite involved different consecutive steps; firstly, calculated amount of Iron nitrate under control Nitrogen environment was forced nucleated by Ammonium hydroxide (pH 10) to achieve iron hydroxide nuclei in a solution.

$Fe(NO)_3 + NH_4OH \rightarrow Fe(OH)_3 + NH_4NO_3$

**2.1.2 Condensation:** The obtained gel was later filtered and washed with water and ethanol, with high speed centrifuge machine accordingly. It was later left overnight under organic solvent to stop and control the size of formed nuclei.

**2.1.3 Calcination process:** The sample was dried in the oven at 100 °C for 2 hours followed by calcination at 350 °C in a muffle furnace under static air environment for 20min. This is done for the reduction of the sample in order to get our desired product. The sample is then air cooled and transferred into a washed, clean and dried vile (Hu, Percheron, Chaumont, & Brachais, 2011).

$Fe(OH)_3 \rightarrow \gamma\ Fe_2O_3 + \alpha Fe_2O_3$

### 2.2 Preparation of 1% zn doped maghemite:

**2.2.1 Hydrolysis:** The formation of Zn doped maghemite nanoparticles involves different sequential steps. Calculated amount of Iron Nitrate and doped material (1%) Zinc nitrate under nitrogen environment were forced nucleated by ammonium hydroxide to form a super saturated solution, to produce the Zn-Fe hydroxide solution.

$Fe(NO)_3 + Zn + 2NH_4OH \rightarrow ZnFe(OH)_2 + 2NH_4Cl$

**2.2.2 Condensation:** Next step involved an immediate condensation which leads to the formation of three-dimensional gels. The obtained gel was later filtered and washed with water and ethanol with high speed centrifuge machine. The sample was left overnight to achieve maximum (size controlled) nuclei sizes.

**2.2.3 Calcination process:** The sample was dried in the oven at 100 °C for 2 hours followed by calcination at 350 °C in a muffle furnace under static air environment for 20min. This is done for the reduction of the sample in order to get our

desired product. The sample is then air cooled and transferred into a washed, clean and dried vile (Khalil, Mahmoud, & Ali, 2008).

$Zn.Fe(OH)_2 \rightarrow Zn.Fe_2O_3 + H_2O$

**2.3 Preparation of 2% zn doped maghemite**:

**2.3.1 Hydrolysis:** The formation of Zn doped maghemite nanoparticles involves different sequential steps. Calculated amount of Iron Nitrate and doped material (2%) Zinc nitrate under nitrogen environment were forced nucleated by ammonium hydroxide to form a super saturated solution, to produce the Zn-Fe hydroxide solution.

$Fe(NO)_3 + Zn + 2NH_4OH \rightarrow ZnFe(OH)_2 + 2NH_4Cl$

**2.3.2 Condensation:** Next step involved an immediate condensation which leads to the formation of three-dimensional gels. The obtained gel was later filtered and washed with water and ethanol with high speed centrifuge machine. The sample was left overnight to achieve maximum (size controlled) nuclei sizes.

**2.3.3 Calcination process:** The sample was dried in the oven at 100 °C for 2 hours followed by calcination at 350 °C in a muffle furnace under static air environment for 20min. This is done for the reduction of the sample in order to get our desired product. The sample is then air cooled and transferred into a washed, clean and dried vile (Drofenik, Kristl, Makovec, Jagličić, & Hanžel, 2008).

$Zn.\ Fe(OH)_2 \rightarrow Zn.Fe_2O_3 + H_2O$

**2.4 Preparation of 3% Zn doped maghemite:**

**2.4.1 Hydrolysis**: The formation of Zn doped maghemite nanoparticles involves different sequential steps. Calculated amount of Iron Nitrate and doped material (3%) Zinc nitrate under nitrogen environment were forced nucleated by ammonium hydroxide to form a super saturated solution, to produce the Zn-Fe hydroxide solution.

$Fe(NO)_3 + Zn + 2NH_4OH \rightarrow ZnFe(OH)_2 + 2NH_4Cl$

**2.4.2 Condensation:** Next step involved an immediate condensation which leads to the formation of three-dimensional gels. The obtained gel was later filtered and washed with water and ethanol with high speed centrifuge machine. The sample was left overnight to achieve maximum (size controlled) nuclei sizes.

**2.4.3 Calcination process**: The sample was dried in the oven at 100 °C for 2 hours followed by calcination at 350 °C in a muffle furnace under static air environment for 20min. This is done for the reduction of the sample in order to get our desired product. The sample is then air cooled and transferred into a washed, clean and dried vile.

$Zn.Fe(OH)_2 \rightarrow Zn.Fe_2O_3 + H_2O$

**2.5 Characterization tools:**

Some basic Nanoparticles characterization techniques are:

I. X-ray diffraction technique (XRD)
II. Vibrating sample magnetometer (VSM)
III. Scanning Electron Microscope (SEM).

**2.5.1 X-RAY Diffraction Technique (XRD):** Information of phase identification is provided by XRD, crystal size and crystal perfection, structural parameters (Edge, length and unit cell) and degree of substitution of ions by other ions. Structured characterization (crystallinity and phase analysis) of synthesized products were conducted by X-ray diffraction using Rigaku Geiger flux instrument (Dmax-IIIA) with Cu kα radiation. The XRD data were received in the 2@ range of 10 °C- 70°Cat the scan rate of 3°/min. A horizontal assembly dilatometer (NETZSCH 409) was used to observe the reduction behavior (Ali, Chiang, & Santos, 2022).

**2.5.2 Vibrating Samples Magnetometry (VSM):** A vibrating-sample magnetometer (VSM) (also referred to as a Foner magnetometer) is a scientific instrument that measures magnetic properties A sample is first magnetized in a uniform magnetic field. It is then sinusoidally vibrated, typically through the use of a piezoelectric material. Commercial systems use linear actuators of some form. Historically, these systems were developed using modified audio speakers, though this approach was dropped due to the interference through the produced in-phase magnetic noise, as

the magnetic flux through a nearby pickup coil varies sinusoidally. The induced voltage in the pickup coil is proportional to the sample's magnetic moment, but does not depend on the strength of the applied magnetic field. In a typical setup, the induced voltage is measured with a lock-in amplifier using the piezoelectric signal as a frequency reference. It is also possible to record the hysteresis curve of a material by sweeping the magnetic field (Foner, 1956).

**2.5.3 Scanning Electron Microscope (SEM)**: The characterization of Scanning electron microscope examination is active to find out the size, shape & morphologies of formed nanoparticle. A desired image of sample surface along with high resolution is provide by SEM. The scanning electron microscope mechanism as same standard as an optical microscope, but it measures the electrons dispersed from the sample instead photon. The wavelength can be shorter than the photons due to acceleration of electrons by electric potential. This marks the SEM capable of telescopic images up to 200.000 times. Measures the particle size and characterization, conductive or sputter coated sample are involved and the sensitivity down to 1nm A SEM (Scanning Electron Microscope) is a kind of electron microscope. Scanning the surface with a targeted beam of electrons, SEM produces images of a sample. SEM is a tool to study a three dimensional image of the specimen. When the primary accelerated electrons strike the sample, the secondary electron is formed. These secondary electrons are received by a positive charged electron detector, which in turn provides a three-dimensional image of the sample (Mayeen, Shaji, Nair, & Kalarikkal, 2018).

**3. Results:**

**3.1 X-ray diffraction technique (XRD):** The X-ray diffraction (XRD) patterns spectrum were employed to determine the phase, crystallinity and composition of doped Nano-crystal.

**3.1.1 XRD result of 1 % zinc dopped maghemite nanoparticles:**

The XRD patterns were obtained for the 1% Zinc doped maghemite samples. In table 1, observed at d-spacing values of 2.53, 2.39 and 2.03 in all samples correspond to cubic phase of Maghemite nanoparticles. The presence of the satellite peak (fig 1) at ˜30˜40 [2 Theta], distinguishes clearly that the sample contain only maghemite and the particles are predominantly Maghemite nanoparticles. The crystal structure of nanoparticles was analyzed by X-ray diffraction (XRD). The Scherrer formula (Khanna & Verma, 2013) was used to calculate the crystallite size of the prepared catalyst. By using Scherrer formula, we can measure the size of nanoparticles.

$D=K\lambda/\beta\cos\theta$ Where, D is crystallite size is shape factor, K=0.94 is scherrer constant $\lambda$=1.54A is the X-ray wavelength for Cu k$\alpha$, $\beta$ is the peak broadening at half maximum and $\theta$ is the Bragg angle.

Where, $\lambda$ for [Å]=1.54060 K= 0.94 The average size of nanoparticle is found to be 14.6nm.

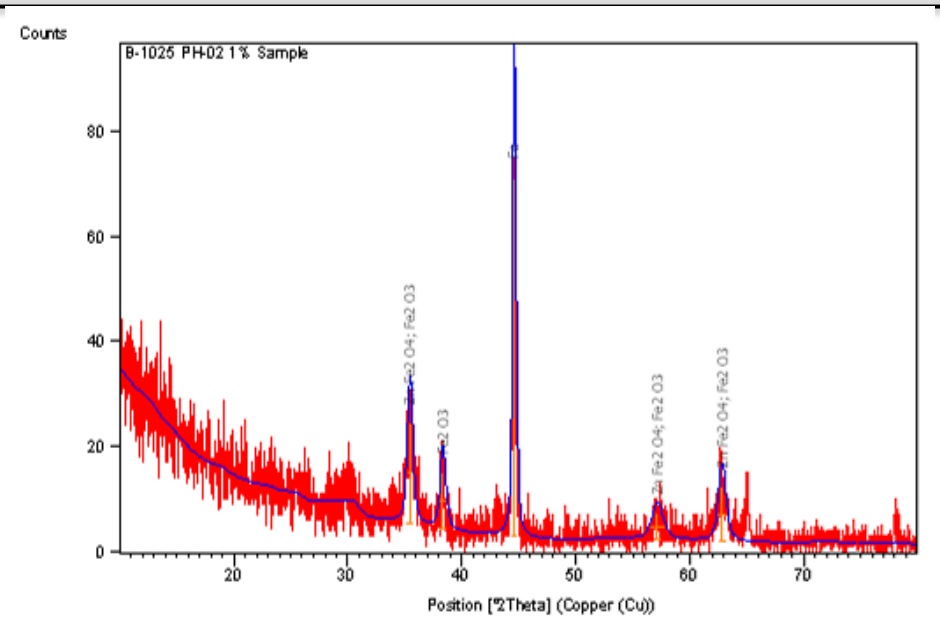


**Fig 1: Shows the X-ray diffraction pattern of the 1% Zn Doped Maghemite**

**Table 1: Size of 1% Zn doped nano particles individually**

| Peak Position [°2Th.] | FWHM [°2Th.] | d- spacing [Å] | Particle Size (nm) |
|---|---|---|---|
| 35.45512 | 0.5904 | 2.53189 | 14.1 |
| 38.32703 | 0.5904 | 2.34852 | 14.2 |
| 44.58639 | 0.3444 | 2.03228 | 24.9 |
| 57.1573 | 1.1808 | 1.61161 | 7.7 |
| 62.80787 | 0.7872 | 1.47953 | 11.8 |
| Average Particle Size | | | 14.6 |

**3.1.2 XRD result of 2 % Zinc dopped maghemite nanoparticles:**

The XRD pattern was obtained for the 2% zinc doped iron oxide samples. The peak observed at d-spacing values of 2.80, 2.71 and 2.46 in all samples corresponding to wurtzite phase of Zinc ferrite oxide nanoparticles.

The presence of the satellite peak in fig and table 2 at ˜30˜36[2 theta], distinguished clearly that the sample contains only maghemite state and there are no signs of hematite peaks. It shows that we have successfully doped zinc in maghemite molecules in a crystal lattice.

The crystal structure of Zinc ferrite oxide nanoparticles was analysed by X-ray diffraction (XRD). The Scherrer formula (Khanna & Verma, 2013) was used to calculate the crystallite size of the prepared catalyst.

By using Scherrer formula, we can measure the size of nanoparticles.

$$D=K\lambda/\beta\cos\theta$$

Where, D is crystallite size is shape factor, K=0.94 is scherrer constant λ=1.54A is the X-ray wavelength for Cu kα, β is the peak broadening at half maximum and θ is the Bragg angle.

Where, λ for [Å]=1.54060 K= 0.94

The average size of nanoparticle is found to be 22nm.

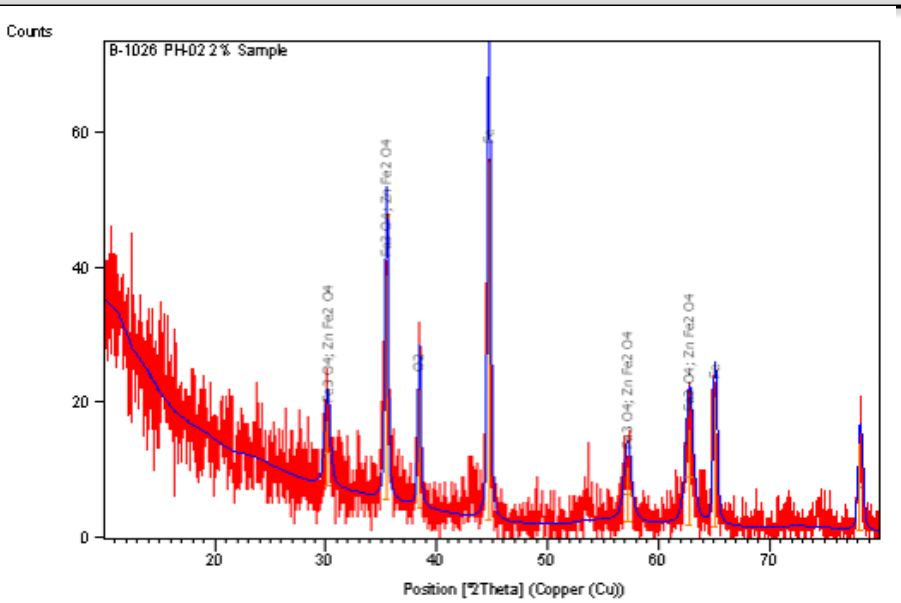


**Figure 2: XRD Diffraction patterns of 2% Zinc Oxide doped maghemite**

**Table 2: Size of 2% Zn doped maghemite nano particles individually**

| Peak Position [°2Th.] | FWHM [°2Th.] | d- spacing [Å] | Particle Size (nm) |
|---|---|---|---|
| 30.1181 | 0.5904 | 2.96726 | 13.9 |
| 35.46351 | 0.2952 | 2.53131 | 28.2 |
| 38.41704 | 0.2952 | 2.34322 | 28.5 |
| 44.69262 | 0.2952 | 2.02769 | 29.1 |
| 57.19945 | 0.7872 | 1.61052 | 11.5 |
| 62.75007 | 0.7872 | 1.48076 | 11.8 |
| 65.08792 | 0.3444 | 1.43311 | 27.4 |
| 78.16286 | 0.3936 | 1.22289 | 26.0 |

### 3.1.3 XRD result of 3 % zinc dopped maghemite nanoparticles

The XRD pattern was obtained for the 3% zinc doped iron oxide samples. The peak observed at d-spacing values of 2.80, 2.71 and 2.46 in all samples corresponding to wurtzite phase of Zinc ferrite oxide nanoparticles.

The presence of the satellite peak in fig (3) at ~30~36[2 theta], distinguished clearly that the sample contains only maghemite state and there are no signs of hematite peaks. It shows that we have successfully doped zinc in maghemite molecules in a crystal lattice.

The crystal structure of Zinc ferrite oxide nanoparticles was analysed by X-ray diffraction (XRD). The Scherrer formula (Khanna & Verma, 2013) was used to calculate the crystallite size of the prepared catalyst.

By using Scherrer formula, we can measure the size of nanoparticles.

$$D=K\lambda/\beta\cos\theta$$

Where, D is crystallite size is shape factor, K=0.94 is scherrer constant λ=1.54A is the X-ray wavelength for Cu kα, β is the peak broadening at half maximum and θ is the Bragg angle.

Where, λ for [Å]=1.54060 K= 0.94

The average size of nanoparticle is found to be 19.4 nm

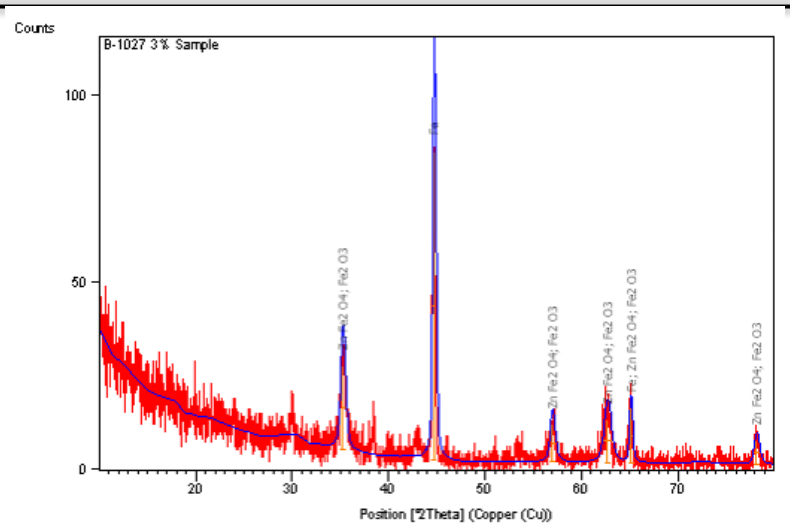


**Figure 2: XRD Diffraction patterns of 3% Zinc Oxide doped maghemite**

**Table 2: Size of 2% Zn doped maghemite nano particles individually**

| Peak Position [°2Th.] | FWHM [°2Th.] | d- spacing [Å] | Particle Size (nm) |
|---|---|---|---|
| 35.26567 | 0.5904 | 2.54505 | 14.1 |
| 44.72148 | 0.3444 | 2.02645 | 24.9 |
| 57.00821 | 0.5904 | 1.61547 | 15.3 |
| 62.70259 | 0.8856 | 1.48176 | 10.5 |
| 65.11488 | 0.2952 | 1.43258 | 31.9 |
| 78.15031 | 0.5904 | 1.22305 | 19.4 |
| Average Particle Size | | | 19.4 |

### 3.2 VIBRATING SAMPLE MAGNETOMETERY (VSM)

A vibrating sample magnetometer (VSM) was used to measure magnetic properties of the samples at room temperature.

#### 3.2.1 VSM analysis of 1% Zn doped maghemite

Hysteresis loops of 1% Zn doped maghemite nanoparticles, were characterized by a vibrating sample magnetometer (VSM) as a function of the magnetic field at room temperature (Figure 4).

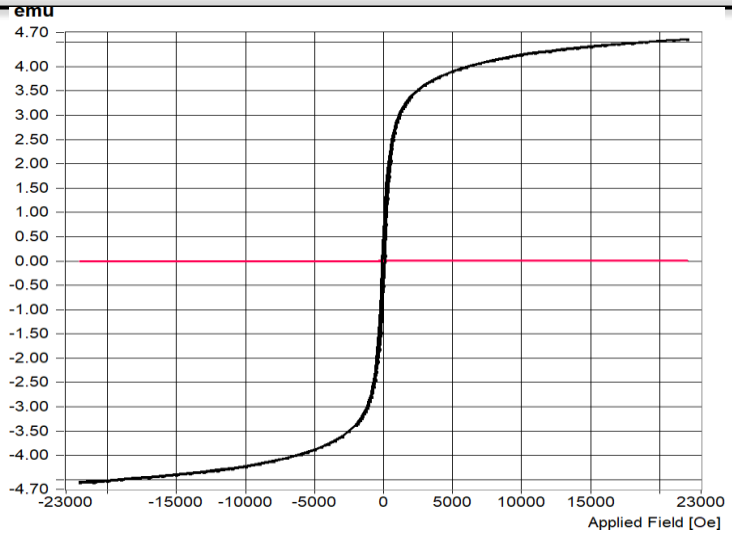


**Figure 4: Hysteresis loop of 1% Zn doped Maghemite**

The values of saturation magnetization (Ms), remanent magnetization (Mr) and high coercivity (*H*ci) are shown in Table 4.

**Table 4:** parameters of 1% Zinc doped maghemite

| Ms (emu) | Mr (emu) | Hc (Oe) | S |
|---|---|---|---|
| **4.563** | 5.53E-01 | 87.733 | 0.12 |

The saturation magnetization of magnetic iron oxide nanoparticles was about 4.563 emu, the remanent was 5.53E-01 emu, high coercivity was 87.733 Oe. This shows the superparamagnetic behavior.

**3.2.2 VSM analysis of 2% Zn doped maghemite:**

Hysteresis loops of 1% Zn doped maghemite nanoparticles, were characterized by a vibrating sample magnetometer (VSM) as a function of the magnetic field at room temperature (Figure 5).

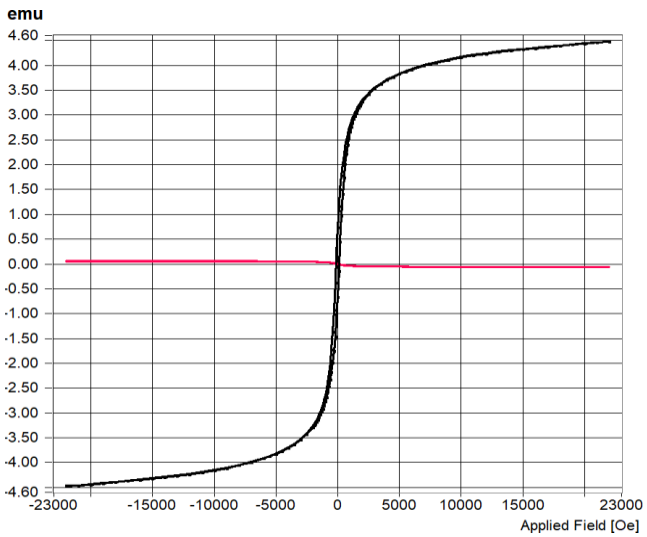


**Figure 5: Hysteresis loop of 2% Zn doped Maghemite**

The values of saturation magnetization (Ms), remanent magnetization (Mr) and high coercivity (*H*ci) are shown in Table 5.

**Table 5: parameters of 2% zinc doped maghemite**

| Ms (emu) | Mr (emu) | Hc (Oe) | S |
|---|---|---|---|
| **4.474** | 7.04E-01 | 129.526 | 0.16 |

The saturation magnetization of magnetic iron oxide nanoparticles was about 4.474 emu, the remanent was 7.04E-01 emu, high coercivity was 129.526 Oe. This shows the superparamagnetic behavior.

**3.2.3 VSM analysis of 3% Zn doped maghemite:** Hysteresis loops of 3% Zn doped maghemite nanoparticles, were characterized by a vibrating sample magnetometer (VSM) as a function of the magnetic field at room temperature (Figure 6).

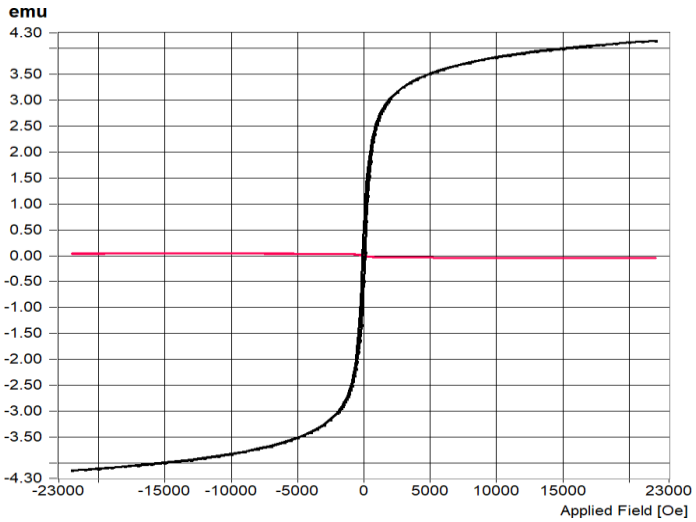


**Figure 6: Hysteresis loop of 3% Zn doped Maghemite**

The values of saturation magnetization (Ms), remanent magnetization (Mr) and high coercivity (*H*ci) are shown in Table 5.

**Table 6: parameters of 3% zinc doped maghemite**

| Ms (emu) | Mr (emu) | Hc (Oe) | S |
|---|---|---|---|
| **4.149** | 5.26E-01 | 92.73 | 0.13 |

The saturation magnetization of magnetic iron oxide nanoparticles was about 4.149 emu, the remanent was 5.26E-01 emu, and high coercivity was 92.73 Oe. This shows the superparamagnetic behavior.

**3.3 SCANNING ELECTRON MICROSCOPE (SEM):**

The morphology of the synthesized Zn doped maghemite nanoparticles was studied by SEM. Shows in the SEM images of the nanoparticles size in the range 30nm-50nm. In (fig 7, 8 and 9) show is the indication that Zn doped maghemite nanoparticles were successfully achieved.

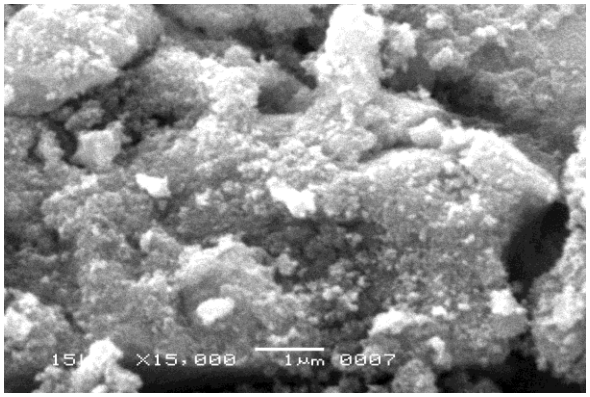


**Figure 7: SEM image of 1% Zn doped maghemite nanoparticles**

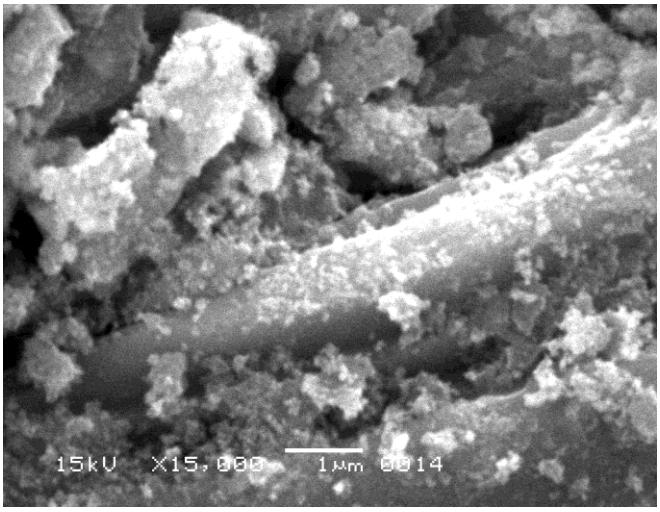


**Figure 8: SEM image of 2% Zn doped maghemite nanoparticles**

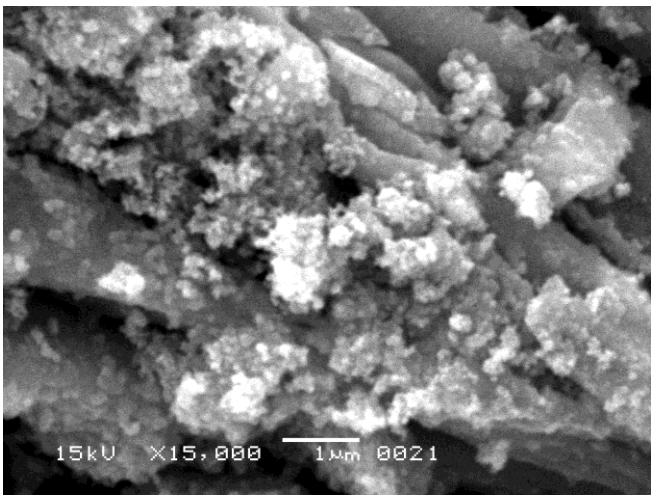


**Figure 9: SEM image of 3% Zn doped maghemite nanoparticles**

### 3.4 Catalytic reaction:

In a typical run, initial solution contains 0.798 %m/m Sulphur content in a diesel fuel, as calculated by X-RF technique. The oxidative desulphurization experiment was performed in three different beakers including for 1%, 2% and 3% nanoparticles. These are fitted in condenser with magnetic stirrer and immersed in a water bath with a temperature controller. Each beaker contained 10 ml diesel fuel, whereas catalyst and hydrogen peroxide were introduced once the temperature attained at 80°C, under atmospheric pressure for two hours' time, at high stirring rate.

Then the liquid sample was transferred to a separating funnel followed by the addition of extracting solvent and mix thoroughly.

The hydrocarbon layer of simulated oil solution is then separated subjected to qualitative and quantitative analysis.

### 3.5 Analysis of product:

The hydrocarbon part of the liquid after extraction will determine the Sulphur content. The ASTM standard D- 4294 method was used and executes this method in XRF instrument. After experimental work Sulphur content removed in diesel fuel is tabulated in table 6

**Table 6: Percentage of Zn doping in maghemite with sulfure content of diesel**

| Percentage of Zn doping in maghemite | sulfur content of diesel after reaction | Percentage of desulfurization |
|---|---|---|
| 1% | 0.399 | 50% |
| 2% | 0.344 | 57% |
| 3% | 0.2793 | 65% |

Therefore, the percentage removal was observed to be very high, which is almost 87%, as calculated by X-RF technique.

The results showed that with the increase in percent of doping of Zn in the maghemite the sulfur content removal has been increased figure 10.

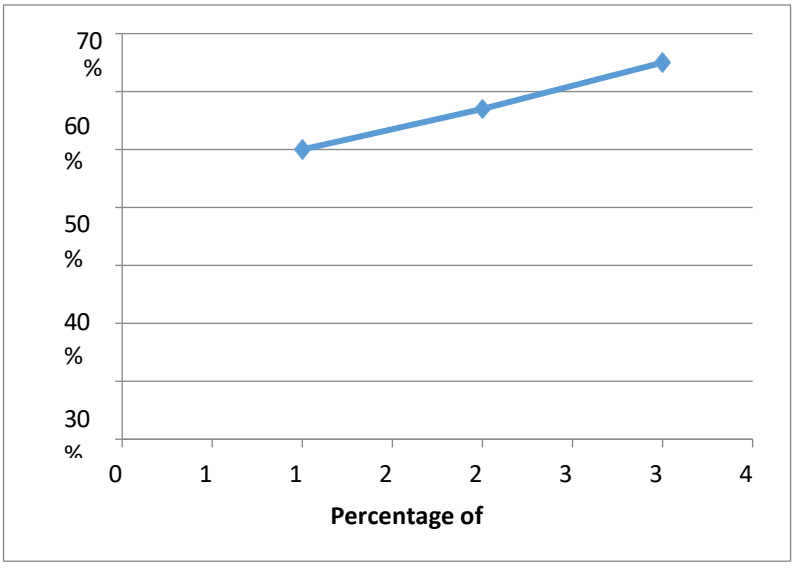


**Figure 10: shows a gradual increase in sulfur removal as doping of Zn is increased**

### 3.6 Catalyst reusability:

After the completion of the reaction, the reaction solution above the solid catalyst was completely decanted. Then, a fresh solution of the required

volume of diesel fuel containing Sulphur content was added and the reaction was repeated in the presence of similar amount of newly added $H_2O_2$ solution.

**Discussion:**

The structural, magnetic, and catalytic properties of Zn-doped maghemite nanoparticles reveal a strong dependence on dopant concentration, demonstrating that Zn incorporation effectively tunes the physicochemical characteristics of the system for catalytic applications. X-ray diffraction analysis confirms that all synthesized samples retain the cubic spinel structure of γ-$Fe_2O_3$ with no detectable impurity phases such as hematite, indicating high phase purity and successful synthesis. The preservation of characteristic diffraction peaks across all doping levels suggests that $Zn^{2+}$ ions are incorporated into the maghemite lattice without disrupting its fundamental framework. However, slight shifts in peak positions and variations in d-spacing at higher doping levels indicate lattice distortion due to substitution of $Fe^{3+}$ ions by $Zn^{2+}$ ions, which possess a larger ionic radius. This substitution induces internal strain and modifies the crystal environment, as reflected in peak broadening.

$$D = \frac{K\lambda}{\beta \cos}$$

The crystallite size calculated using the Scherrer equation exhibits a non-linear trend, increasing at intermediate doping (2%) and decreasing at higher doping (3%). This behavior suggests that moderate Zn incorporation facilitates crystal growth, possibly by reducing lattice energy, whereas excessive doping introduces structural defects that hinder crystallite development. Such defect formation is advantageous for catalytic activity, as it enhances the number of active sites available for reaction.

Magnetic measurements further support the influence of Zn doping on the internal structure of the nanoparticles. All samples exhibit superparamagnetic-like behavior, characterized by low coercivity and remanence, which is typical of nanoscale ferrimagnetic systems. The observed decrease in saturation magnetization with increasing Zn content can be attributed to the substitution of magnetic $Fe^{3+}$ ions with non-magnetic $Zn^{2+}$ ions. In spinel structures, $Zn^{2+}$ preferentially occupies tetrahedral sites, displacing $Fe^{3+}$ ions and weakening the superexchange interactions between tetrahedral and octahedral sites. This redistribution reduces the overall magnetic moment of the system. The variation in coercivity, particularly the increase at intermediate doping followed by a decrease at higher doping, reflects the interplay between particle size, magnetic anisotropy, and structural disorder. The consistently low squareness ratio across all samples confirms their superparamagnetic nature, which is beneficial for catalyst recovery using an external magnetic field.

Morphological analysis through SEM reveals quasi-spherical nanoparticles with noticeable agglomeration, which is expected due to magnetic dipole–dipole interactions and high surface energy. The observed particle sizes are larger than the crystallite sizes obtained from XRD, indicating that the particles are composed of multiple crystallites aggregated together. While agglomeration may reduce the effective surface area, it can also facilitate interparticle interactions that enhance catalytic performance. The morphology remains relatively consistent across different doping levels, suggesting that Zn incorporation does not significantly alter the growth mechanism but may influence surface properties.

The catalytic performance in oxidative desulfurization demonstrates a clear improvement with increasing Zn doping, indicating that Zn plays a crucial role in enhancing catalytic activity. The increase in sulfur removal efficiency with higher Zn content can be explained by modifications in the electronic structure and surface chemistry of the catalyst. Zn incorporation promotes redox cycling between $Fe^{2+}$ and $Fe^{3+}$, facilitating the activation of hydrogen peroxide, which acts as the oxidizing agent. Additionally, the introduction of Zn creates oxygen vacancies and structural defects that serve as active sites for adsorption and oxidation of sulfur-containing compounds. The improved catalytic activity at higher doping levels

suggests that defect density and surface reactivity are key factors governing performance. The highest efficiency observed at 3% Zn doping indicates an optimal balance between crystallinity and defect formation, enhancing both adsorption and oxidation processes.

A clear structure property performance relationship is evident, where Zn doping induces lattice distortion and defect formation, modifies magnetic interactions, and enhances catalytic activity. While increased doping improves catalytic efficiency, it simultaneously reduces saturation magnetization, which may affect the ease of magnetic recovery. Therefore, an optimal doping level is necessary to balance catalytic performance with magnetic separability. The overall results suggest that Zn-doped maghemite nanoparticles are effective catalysts for oxidative desulfurization, offering high efficiency under mild operating conditions along with the advantage of magnetic recyclability.

**Conclusion:**

In this study, size-controlled maghemite and Zn-doped maghemite nanoparticles were successfully synthesized, and their structural, magnetic, and catalytic properties were systematically evaluated. XRD analysis confirmed the formation of phase-pure cubic maghemite with successful Zn incorporation into the lattice, leading to lattice distortion and modification of crystallite size. The observed variation in crystallite size with increasing Zn content highlights the dual role of doping in promoting crystal growth at lower concentrations and inducing structural defects at higher concentrations. Magnetic characterization demonstrated that all samples exhibit superparamagnetic behavior with low coercivity and remanence, which is favorable for magnetic separation. The gradual decrease in saturation magnetization with increasing Zn doping was attributed to the substitution of magnetic $Fe^{3+}$ ions with non-magnetic $Zn^{2+}$ ions and the resulting cation redistribution within the spinel structure. The catalytic performance in oxidative desulfurization revealed a significant enhancement in sulfur removal efficiency with increasing Zn content, indicating that Zn doping plays a crucial role in improving catalytic activity. This enhancement is associated with increased surface defects, improved redox properties, and enhanced interaction with sulfur-containing compounds. Among the studied compositions, higher Zn doping exhibited superior catalytic efficiency, suggesting an optimal balance between structural defects and catalytic activity. Furthermore, the magnetic recoverability of the nanoparticles ensures easy separation and reusability, making them highly suitable for practical applications. Overall, the findings establish a clear correlation between Zn doping, structural modification, magnetic behavior, and catalytic performance, highlighting Zn-doped maghemite nanoparticles as efficient, stable, and recyclable catalysts for environmental remediation, particularly in oxidative desulfurization processes.

**REFERENCES:**

Aflori, M. (2021). Smart nanomaterials for biomedical applications—a review. *Nanomaterials, 11*(2), 396.

Ahamed, M., Ali, S. M., Lateef, R., Dotto, G. L., & Alhadlaq, H. A. Results in Engineering.

Ahmed, S. I., & Sanad, M. M. (2021). Maghemite-based anode materials for Li-Ion batteries: The role of intentionally incorporated vacancies and cation distribution in electrochemical energy storage. *Journal of Alloys and Compounds, 861*, 157962.

Al Kindi, U. S. H. (2020). *Tuning Structural, Electronic, and Magnetic Properties of Nanocrystalline Iron Oxides and Fe-Carbon Nanotubes Composites*: Sultan Qaboos University (Oman).

Ali, A., Chiang, Y. W., & Santos, R. M. (2022). X-ray diffraction techniques for mineral characterization: A review for engineers of the fundamentals, applications, and research directions. *Minerals, 12*(2), 205.

Anik, M. I., Hossain, M. K., Hossain, I., Mahfuz, A., Rahman, M. T., & Ahmed, I. (2021). Recent progress of magnetic nanoparticles in biomedical applications: A review. *Nano Select, 2*(6), 1146-1186.

Bashir, U., & Shahid, M. (2026). Nanoparticle-Based Interventions Targeting Dysregulated Neuronal Signaling in Neurodegenerative Disorders *Nanoparticles Agents and Secondary Metabolites in Neurodegenerative Diseases* (pp. 387-426): IGI Global Scientific Publishing.

Bokov, D., Turki Jalil, A., Chupradit, S., Suksatan, W., Javed Ansari, M., Shewael, I. H., . . . Kianfar, E. (2021). Nanomaterial by sol-gel method: synthesis and application. *Advances in materials science and engineering, 2021*(1), 5102014.

Bruno, F., Granata, V., Cobianchi Bellisari, F., Sgalambro, F., Tommasino, E., Palumbo, P., . . . Brunese, M. C. (2022). Advanced magnetic resonance imaging (MRI) techniques: technical principles and applications in nanomedicine. *Cancers, 14*(7), 1626.

Castellanos-Rubio, I., Arriortua, O., Marcano, L., Rodrigo, I., Iglesias-Rojas, D., Barón, A., . . . Fdez-Gubieda, M. L. (2021). Shaping up zn-doped magnetite nanoparticles from mono-and bimetallic oleates: the impact of Zn content, Fe vacancies, and morphology on magnetic hyperthermia performance. *Chemistry of Materials, 33*(9), 3139-3154.

Chaudhari, D. S., Upadhyay, R. P., Shinde, G. Y., Gawande, M. B., Filip, J., Varma, R. S., & Zbořil, R. (2024). A review on sustainable iron oxide nanoparticles: syntheses and applications in organic catalysis and environmental remediation. *Green Chemistry, 26*(13), 7579-7655.

Dhahri, R., Benamara, M., Bouzidi, S., Ben Moussa, S., Alzahrani, A. Y. A., Nassar, K. I., . . . Al-Syadi, A. (2025). Effect of Gd doping on the microstructure and electrical characteristics of Maghemite ($\gamma$-$Fe_2O_3$) ceramics. *Journal of Sol-Gel Science and Technology, 113*(1), 225-242.

Drofenik, M., Kristl, M., Makovec, D., Jagličić, Z., & Hanžel, D. (2008). Sonochemically assisted synthesis of zinc-doped maghemite. *Ultrasonics sonochemistry, 15*(5), 791-798.

Duglet, R., Sharma, D., Singh, V., Sharma, D., & Singh, M. (2025). Temperature-driven evolution of hematite (α-Fe2O3) nanoparticles: A study on structural, morphological and magnetic properties. *Solid State Communications, 396*, 115761.

Elmacı, G., Özgenç, G., Kurz, P., & Zumreoglu-Karan, B. (2020). Enhanced water oxidation performances of birnessite and magnetic birnessite nanocomposites by transition metal ion doping. *Sustainable Energy & Fuels, 4*(6), 3157-3166.

Foner, S. (1956). Vibrating sample magnetometer. *Review of Scientific Instruments, 27*(7), 548-548.

Halbreich, A., Roger, J., Pons, J., Geldwerth, D., Da Silva, M., Roudier, M., & Bacri, J. (1998). Biomedical applications of maghemite ferrofluid. *Biochimie, 80*(5-6), 379-390.

Hu, L., Percheron, A., Chaumont, D., & Brachais, C.-H. (2011). Microwave-assisted one-step hydrothermal synthesis of pure iron oxide nanoparticles: magnetite, maghemite and hematite. *Journal of sol-gel science and technology, 60*(2), 198-205.

Islam, M. B., Pavel, M. R., Islam, M. R., & Haque, M. J. (2022). Synthesis of Cobalt Ferrite Nanoparticles using microemulsion method: Structure, morphology, and magnetic properties. *Journal of Engineering Science, 13*(1), 81-87.

Khalil, Mahmoud, H. A., & Ali, T. T. (2008). Direct formation of thermally stabilized amorphous mesoporous Fe2O3/SiO2 nanocomposites by hydrolysis of aqueous iron (III) nitrate in sols of spherical silica particles. *Langmuir, 24*(3), 1037-1043.

Khan, M. Y., Gupta, P., & Verma, V. K. (2013). A review-biomedical engineering-present and future prospective. *Asian J. Pharm. Res, 3*(4), 202-206.

Khandaker, T., Anik, M. A. A. M., Nandi, A., Islam, T., Islam, M. M., Hasan, M. K., . . . Hossain, M. S. (2025). Recent progress in gel catalysts: boosting efficiency for sustainable energy applications. *Catalysis Science & Technology, 15*(5), 1357-1389.

Khanna, L., & Verma, N. (2013). Size-dependent magnetic properties of calcium ferrite nanoparticles. *Journal of Magnetism and Magnetic Materials, 336*, 1-7.

Khanvilkar, M. B., Nikumbh, A. K., Pawar, R. A., Karale, N. J., Nagwade, P. A., Nighot, D. V., . . . Panchgalle, S. P. (2023). Effect of divalent/trivalent doping on structural, electrical and magnetic properties of spinel ferrite nanoparticles. *Engineered Science, 22*(3), 850.

Lee, C.-H., Chin, H.-H., Zeng, K.-Y., Chang, Y.-J., Yeh, A.-C., Yeh, J.-W., . . . Huang, E.-W. (2022). Tailoring Ferrimagnetic Transition Temperatures, Coercivity Fields, and Saturation Magnetization by Modulating Mn Concentration in (CoCrFeNi) 1− x Mn x High-Entropy Alloys. *Frontiers in Materials, 9*, 824285.

Ma, Z., Mohapatra, J., Wei, K., Liu, J. P., & Sun, S. (2021). Magnetic nanoparticles: synthesis, anisotropy, and applications. *Chemical reviews, 123*(7), 3904-3943.

Mayeen, A., Shaji, L. K., Nair, A. K., & Kalarikkal, N. (2018). Morphological characterization of nanomaterials *Characterization of nanomaterials* (pp. 335-364): Elsevier.

Mazen, S., Abu-Elsaad, N., & Nawara, A. (2020). The influence of various divalent metal ions (Mn2+, Co2+, and Cu2+) substitution on the structural and magnetic properties of nickel–zinc spinel ferrite. *Physics of the Solid State, 62*(7), 1183-1194.

Mugisha, A. I. (2024). *Synthesis and application of multifunctional iron oxide-graphene oxide nanocomposite materials for sulfur pollutant removal.* Université d'Ottawa | University of Ottawa.

Nisticò, R., Cesano, F., & Garello, F. (2020). Magnetic materials and systems: Domain structure visualization and other characterization techniques for the application in the materials science and biomedicine. *Inorganics, 8*(1), 6.

Salih, S. J., & Mahmood, W. M. (2023). Review on magnetic spinel ferrite (MFe2O4) nanoparticles: From synthesis to application. *Heliyon, 9*(6).

Skandalakis, G. P., Rivera, D. R., Rizea, C. D., Bouras, A., Jesu Raj, J. G., Bozec, D., & Hadjipanayis, C. G. (2020). Hyperthermia treatment advances for brain tumors. *International Journal of Hyperthermia, 37*(2), 3-19.